Chemical Engineering Journal 379 (2020) 122317

Contents lists available at ScienceDirect

Chemical Engineering Journal

journal homepage: www.elsevier.com/locate/cej

Uniformly sized hollow microspheres loaded with polydopamine nanoparticles and doxorubicin for local chemo-photothermal combination therapy

Guoli Ni[a,1], Guang Yang[b,1], Yang He[a], Xilin Li[a], Tianyi Du[a], Ling Xu[a], Shaobing Zhou[a,*]

[a] Key Laboratory of Advanced Technologies of Material, Minister of Education, School of Materials Science and Engineering, Southwest Jiaotong University, Chengdu 610031, Sichuan, PR China

[b] College of Medicine, Southwest Jiaotong University, Chengdu 610031, Sichuan, PR China

HIGHLIGHTS

- A uniformly sized hollow microsphere was developed for enhanced chemo-photothermal combination therapy.
- These microspheres possess high photothermal conversion efficiency and high photostability.
- A high content of drug in the tumor was achieved after intratumoral injection of the microspheres.

GRAPHICAL ABSTRACT

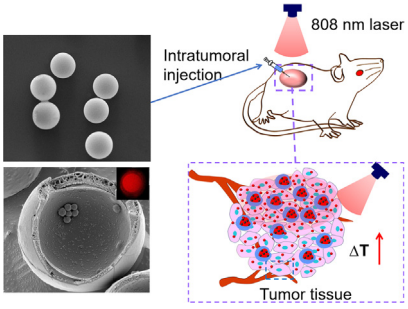

ARTICLE INFO

Keywords:
Nanoparticles
Coaxial electrospraying
Hollow structure
Photothermal therapy
Chemotherapy

ABSTRACT

Techniques to improve the accumulation of therapeutic agents in tumors, which subsequently enhance the therapeutic efficacy of anticancer drugs against malignant tumors and reduce their side effects remains a great challenge. Here, we developed a hollow biodegradable polymer microsphere, in which the interior hollow space was loaded with polydopamine (PDA) nanoparticles and doxorubicin hydrochloride (DOX·HCl) and the outer shell layer was biodegradable polymer poly(lactide-co-glycolide) (PLGA). We produced these microspheres with coaxial electrospraying technology for enhanced local chemo-photothermal combination therapy. The microspheres with a uniform size have high photothermal conversion efficiency and high photostability. When these microspheres were intratumorally injected into tumor-bearing mice, a local hyperthermia effect was immediately generated from the PDA nanoparticles in these microspheres using near-infrared light irradiation at the tumor site. Simultaneously, the loaded DOX·HCl was rapidly released due to photothermy and diffusion into the cells. Compared with intravenously injected nanomedicines, an extremely high content of DOX·HCl in the tumor is achieved, with over ~22% at 6 h after intratumoral injection of the microspheres. Therefore, synergism between the photothermal therapy and chemotherapy will accelerate cell apoptosis, significantly enhance treatment efficacy and decrease the side effects to normal tissues. The intratumoral administration of therapeutic agents possesses more advantages than systemic chemotherapy. The hollow structured microspheres have great potential application as a drug delivery system due to their unique features.

* Corresponding author.
E-mail address: shaobingzhou@swjtu.cn (S. Zhou).
[1] These authors contributed equally to this work.

https://doi.org/10.1016/j.cej.2019.122317
Received 28 April 2019; Received in revised form 14 July 2019; Accepted 22 July 2019
Available online 23 July 2019
1385-8947/

1. Introduction

The main strategies for clinical cancer therapy primarily include surgery, radiotherapy and chemotherapy, which have varying degrees of positive therapeutic effects. However, there are many acute and chronic side effects that adversely impact a patient's overall well-being and cannot be ignored. This is due to the harsh chemicals and radioactive agents used for treatment [1,2]. In comparison, photothermal therapy (PTT), which is an emerging and powerful strategy for cancer therapy, can convert near-infrared (NIR) light into heat to kill tumor cells without damaging normal tissues [3,4]. This strategy is highly selective and minimally invasive [5], because the therapeutic effect only occurs at the tumor site with the accumulation of photothermal agent and exposure to a localized near-infrared (NIR) laser, which effectively decreased the risks discussed above [6,7]. Furthermore, this photo-induced localized hyperthermia therapy also possesses other potential advantages, such as fewer complications, ease of the procedure, faster recovery, and shorter hospital stays [8].

It is highly important to used efficient PTT reagents, which currently focus on inorganic materials, such as noble metal-based nanoparticles (e.g., Au [9], Ag [10,11], and Pd [12]), Cu-based semiconductor nanoparticles (e.g., CuS [3,13] and Cu_2S [14]), carbon-based nanomaterials (e.g., carbon-nanotube [15] and graphene-based agents [16]), and organic materials (e.g., polyaniline nanoparticles [17], porphyrin-based agents [18,19], and polydopamine (PDA)-based nanomaterials [6,20,21]). Despite efficient cancer therapy, the long-term safety of these agents is another extremely important concern. For example, metallic nanoparticles have poor biometabolism and safety- related issues of the metal itself, whereas carbon-based nanomaterials can induce many toxic side effects, such as oxidative stress or pulmonary inflammation [22,23]. Organic materials, particularly naturally existing substances (e.g., porphysomes, melanin) in organisms would be highly beneficial to address these issues, due to their enzymatically biodegradable nature, strong absorption in the NIR region and high photothermal conversion efficiency. Among them, PDA nanoparticles, based on melanin, a widely distributed biopolymer in living organisms with distinct functions [24], including the prevention of ultraviolet injury and thermoregulation, have unique advantages in addition to those discussed, including good biocompatibility, long-term nontoxicity and anticancer efficiency [6,25,26]. Additionally, the fabrication of PDA nanoparticles is simple and cost-effective. Thus, the use of PDA nanoparticles as a photothermal therapeutic agent is an excellent choice for cancer therapy.

However, the widespread clinical use of PTT is still limited mainly due to the lack of tumor-specific energy absorption and diffuse heating, which makes it difficult to sufficiently heat tumors without damaging surrounding tissues [27]. Additionally, incomplete thermal ablation and disease recurrence are common [28]. Therefore, it was important to combine PTT with other therapies to improve cancer therapy. The combination of PTT and chemotherapy was an encouraging approach that will lead to better synergistic effects and lower side effects than photothermal therapy or chemotherapy alone [29–33]. This may be because mild photothermal heating could result in damage to cell membranes, which increases their permeability to enhance the delivery of chemotherapeutic drugs into cancer cells [34,35]. Moreover, minimal tissue hyperthermia will increase blood flow, yielding higher concentrations of chemotherapeutic agents [36].

To effectively realize the combination of PTT and chemotherapy, the photothermal therapeutic agents and chemotherapeutic agents must first be accurately delivered to tumor lesions. However, currently, therapeutic drugs or nanomedicines are mainly delivered to tumor sites *via* systemic administration, such as intravenous injection, which usually requires a higher dose of drug to ensure local drug enrichment at the tumor site. Furthermore, after the nanomedicines or drugs enter blood circulation, numerous barriers exist from the administration site to the target cell, such as mucosal barriers and nonspecific uptake [37,38], resulting in the rapid clearance of drugs with subsequent over accumulation in nontarget organs [39]. As a result, the drugs will damage the normal cells and cause serious side effects in humans [40]. Even if nanocarriers were used to protect drugs from clearance, over-reliance on the enhanced permeation and retention (EPR) effect to deliver them into tumor tissues only leads to a modest increase in tumor enrichment [41]. By contrast, localized drug delivery, which can directly deliver drug into the tumor site in a controlled manner, has such advantages as sparing of off-target tissue toxicities and a relatively reduced dose of chemotherapeutic agents [42]. Several strategies for the local chemotherapy of tumors were previously developed, including antitumor implantable drug delivery systems [43], intrahepatic artery infusion for liver cancer [44], intrapleural infusion for lung cancer [45] and intratumoral cancer chemotherapy [46,47]. These strategies have improved the quality of patient survival in some degree. Among them, intratumoral cancer chemotherapy, especially intratumoral injection is a minimally invasive treatment, which can further increase the specificity of the chemotherapy. However, when the intratumoral injection of free drugs is directly applied, the irregular distribution of drug and rapid clearance continue to occur at the tumor site, resulting in treatments that are highly dependent on the timing and frequency of the drug injections [48]. Therefore, different types of drug carriers, such as *in situ* forming polymer implants [49], *in situ* forming hydrogels [50], and injectable microparticles [51], were used to ensure that the drug is properly localized and that the sustained release of drugs is controlled at the tumor site to maximize the effect of the drug. Because of the burst release of *in situ* forming polymer implants or hydrogels, microparticles are a good choice as an intratumoral drug delivery system. However, there remains a great challenge to simultaneously load PTT nanoparticles and chemotherapeutic agents in a single microsphere.

Accordingly, in this work, we developed a hollow biodegradable polymer microsphere with a coaxial electrospraying technology, which was used as an intratumoral drug delivery system for enhanced chemo-photothermal combination therapy. In contrast to solid microspheres, the hollow structured microsphere with a void space displays many unique features, including high surface area and high loading capacity [52]. The coaxial electrospraying technology was often used for the fabrication of micro/nanoparticles due to the diversity of available polymers, controllable size, high packaging efficiency and encapsulation of hydrophilic and hydrophobic drugs [53]. The size-uniform hollow microsphere (PDA/DOX·HCl@PLGA) was obtained as illustrated in Scheme 1A, in which the interior hollow space was loaded with the polydopamine (PDA) nanoparticles and doxorubicin hydrochloride (DOX·HCl) and the outer shell layer was an oil-soluble polymer poly (lactide-co-glycolide) (PLGA). After the microspheres were intratumorally injected into the tumor-bearing mice, the tumor site was irradiated with an NIR laser (808 nm, 1.5 W/cm^2) (Scheme 1B). Subsequently, local hyperthermia induced by the PDA nanoparticles occurred in tumor tissues, and simultaneously, the loaded DOX·HCl was rapidly released and diffused into the cells. Thus, the synergism of the photothermal therapy and chemotherapy will accelerate cell apoptosis, thereby enhancing the treatment efficacy of this drug against malignant tumors (Scheme 1C).

2. Materials and methods

2.1. Materials

Poly(lactide-co-glycolide) (PLGA, Mw = 54,600 Da) and polydopamine (PDA) nanoparticles were synthesized as our previous report [54,55]. Doxorubicin hydrochloride (DOX·HCl) was purchased from Zhejiang Hisun Pharmaceutical Co., Ltd. (Taizhou, China). Poly(vinyl alcohol) (PVA), dimethyl sulfoxide (DMSO), ethyl acetate (EA), N,N dimethylformamide (DMF), glycerol, and glass slides were purchased from Chengdu Kelong Chemical Reagent Company (China). Propidium iodide (PI) and calcein acetoxymethyl ester (calcein AM) were

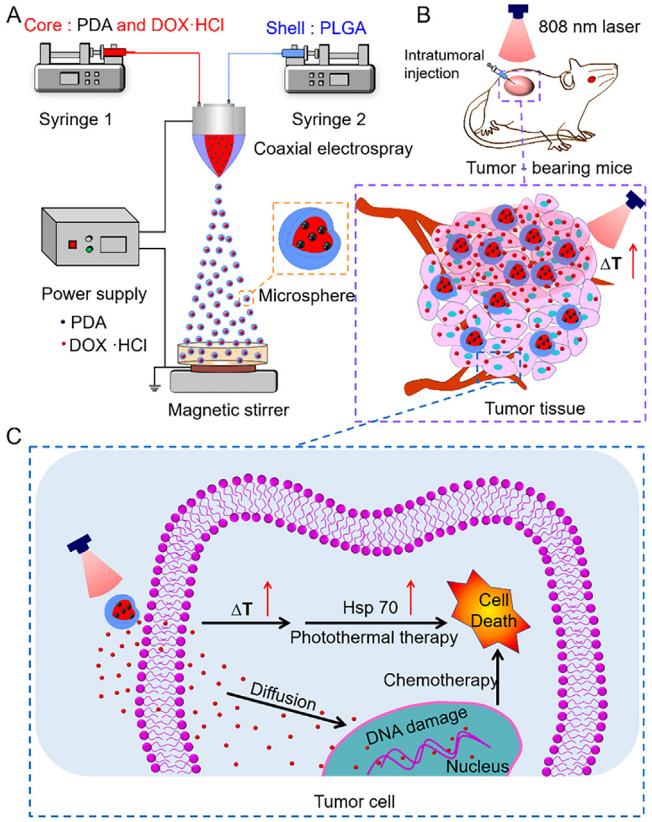

Scheme 1. Schematic diagram of the fabrication of hollow microspheres loaded with both polydopamine nanoparticles and doxorubicin hydrochloride (A). The tumor site of the tumor-bearing mice irradiated with NIR laser (808 nm, 1.5 W/cm^2) after the microspheres were intratumorally injected (B). The synergistic effect of local photothermotherapy and chemotherapy accelerating tumor cell apoptosis (C).

purchased from Biosharp Company. Deionized (DI) water was used in all experiments. Other reagents were used without purification, unless otherwise specified.

2.2. Cell lines

Endothelial cells (ECs) and mouse mammary tumor cell line 4T1 cells were obtained from Sichuan University (Chengdu, China). ECs were cultured in F12 medium (HyClone) supplemented with 10% fetal bovine serum (FBS). 4T1 Cells were cultured in DMEM medium (HyClone) added with 10% FBS. All the cells were cultured at 37°C in a 5% CO_2 atmosphere and 100% humidity.

2.3. Animals

Female BALB/C mice (20 ± 2 g) were feed at the condition of 37 °C and 55% of humidity in Experimental Animal Center of Sichuan University. All animal experiments were approved by the Institutional Animal Care and Use Committee of Sichuan Academy of Medical Sciences and carried out in compliance with guidelines for the Care and Use of Laboratory Animals.

2.4. Preparation of hollow microspheres via coaxial electrospraying

First, the coaxial electrospraying technique was used to fabricate the hollow microspheres. The solution of glycerol and water (2:0.5, v/v) was used as the internal phase solution, and PLGA copolymer (2 g) was dissolved in ethyl acetate (10 mL) as the external phase solution. Subsequently, the process parameters of electrospraying were optimized, including changing the polymer concentration, external flow rate, receiving distance and voltage.

To successfully prepare the hollow microspheres containing PDA nanoparticles, 2 g PDA nanoparticles were dispersed into a 10 mL solution of glycerol and water (2:0.5, v/v) as the internal phase solution. Then, according to the results of the above optimization experiments, the polymer concentration, internal phase flow rate, external phase flow rate, receiving distance, and voltage were adjusted to 20 wt%, 0.2 mL/h, 0.8 mL, 20 cm, and 12 kV, respectively.

Finally, to load both PDA nanoparticles and doxorubicin hydrochloride (DOX·HCl), the PDA nanoparticles and DOX·HCl were dispersed into a solution of glycerol and water as the internal phase solution.

2.5. Characterization of the hollow microspheres

The morphologies of the microspheres were observed by scanning electron microscope (SEM, Quanta 200, FEI, Philips, Netherlands) and several randomly selected areas of images with different magnification were taken from each SEM samples. The SEM images of the samples were analyzed using ImageJ software, and the particle diameters of over 100 microspheres were measured. The polydispersity of the microspheres was evaluated using Formula (1) according to previous reports [56,57],

$$RSD = \frac{1}{\bar{d}}\left[\sum_{i=1}^{n}\frac{(d_i - \bar{d})^2}{n-1}\right]^{\frac{1}{2}} \times 100\% \quad (1)$$

where d_i was the diameter of the microsphere, $\bar{d}$ was the arithmetic mean of the microspheres, and n is the total number of microspheres ($n \geq 100$). The polydispersity index of microspheres was defined as the relative standard deviation (RSD), which was the ratio of the standard deviation to the arithmetic mean of the size distribution, and it can be used to evaluate the polydispersity of the microsphere. A smaller index (RSD) indicates a lower polydispersity of microspheres, primarily a more uniform particle size of the microspheres.

The PDA nanoparticles and the hollow structure of the microspheres containing PDA nanoparticles were visualized by transmission electron microscopy (TEM, JEOL 2100F, JEOL, Ltd., Japan). Cryo-scanning electron microscopy (cryo-SEM, Helios NanoLab G3 UC, Thermo Fisher Scientific, U.S.A) and confocal laser scanning microscopy (CLSM, TCS SP8, Leica, Germany) were also used to further confirm the core-shell structure of the microspheres [58].

2.6. Measurement of photothermal performance

A volume of 3 mL phosphate buffer saline (PBS) and a series of PDA@PLGA aqueous solutions with different concentrations of PGLA (PLGA content: 1, 2, 4 and 8 mg/mL) were irradiated with an 808 nm NIR laser at a power density of 1.5 W/cm^2 for 10 min. Thermal imaging of the samples was performed with an infrared camera at intervals of 2 min. The resulting images were processed with the infrared camera software SmartView. The power density of NIR laser were also tuning from 0.5 to 2.0 W/cm^2 to irradiate the PDA@PLGA aqueous solutions with 4 mg/mL concentration of PLGA. All the solution temperature was monitored with a thermometer and the temperature was recorded every 30 s.

In addition, the photostability of PDA@PLGA was also measured. Briefly, with irradiation on/off cycles, the UV absorbance at 808 nm versus the irradiation time was recorded.

2.7. Characterization of PDA/DOX·HCl-loaded PLGA microspheres

The DOX·HCl loading content (LC) and encapsulation efficiency (EE) were detected with a fluorescence spectrophotometer (F-7000, Hitac, Japan). The lyophilized PDA/DOX·HCl@PLGA microspheres were

dissolved in DMSO. The absorbance of DOX·HCl at 595 nm was measured to quantify the concentration of DOX·HCl in DMSO using a predeveloped calibration curve. Then, the LC and EE of DOX·HCl were calculated according to the following formulas:

$$\text{LC (wt\%)} = \left(\frac{\text{mass of loaded drug}}{\text{mass of drug loaded microspheres}}\right) \times 100\% \quad (2)$$

$$\text{EE (wt\%)} = \left(\frac{\text{mass of loaded drug}}{\text{mass of feeding drug}}\right) \times 100\% \quad (3)$$

The PDA/DOX·HCl @PLGA microspheres were characterized by CLSM to confirm that the DOX·HCl was encapsulated.

2.8. Drug release profiles in vitro with or without NIR laser irradiation

The DOX·HCl release behaviors from PDA/DOX·HCl@PLGA were investigated in phosphate buffer saline (PBS, pH = 6.8). The PDA/DOX·HCl@PLGA (100 mg) was dispersed and immersed in a tube containing 3 mL of PBS. The tube was placed in a shaking bed at 100 rpm at 37 °C. At predetermined time intervals, the tube was centrifuged and 1 mL supernatant was collected for fluorescence spectrophotometer detection to determine the content of released DOX·HCl. After that, 1 mL of fresh PBS solution was supplemented.

To determine the light-triggered drug release kinetics, we also investigated the release of microspheres under NIR laser irradiation. At predetermined time intervals, the samples were irradiated with an 808 nm NIR laser (1.5 W/cm^2) for 10 min. After NIR irradiated, the DOX·HCl contained phosphate buffer saline was collected and replaced with an equal volume of fresh incubation medium as previously described.

2.9. Cytocompatibility assay

The cytocompatibility of PDA@PLGA was evaluated by using both 4T1 and EC cells. To assess the cytocompatibility on these two kinds of cells, 4T1 and EC cells were seeded into 24-well plates at a density of 2×10^4 cells/well, respectively. After attached and well spread, the cells were incubated in culture medium containing PDA@PLGA with different concentrations for another 24 h and washed with PBS for three times. Then they were stained with both calcein AM and propidium iodide (PI) for fluorescence microscopy.

To quantitatively evaluate the cytocompatibility of PDA@PLGA, 4T1 and EC cells were seeded into 96-well plates at a density of 2×10^4 cells/well. After attached and well spread, the cells were incubated in culture medium containing PDA@PLGA with different concentrations for another 24 h and washed with PBS for three times. Then the viability of 4T1 and EC cells were evaluated by the Alamar Blue assay [6,59].

2.10. Photothermal cytotoxicity

Photothermal cytotoxicity of PDA@PLGA was evaluated on both 4T1 and EC cells. To assess the photothermal cytotoxicity on these two kinds of cells, 4T1 and EC cells were incubated in 24-well plates at a density of 2×10^4 cells/well. PDA@PLGA aqueous solutions with different concentrations were added and the cells were further incubated for 30 min. Thereafter, the cells were exposed to an NIR laser (808 nm, 1.5 W/cm^2) for 10 min, then incubated for another 24 h. After that, the cells were stained with both calcein AM and PI.

To quantitatively evaluate the photothermal cytotoxicity of PDA@PLGA, 4T1 and EC cells were incubated in 96-well plates at a density of 2×10^4 cells/well. PDA@PLGA aqueous solutions with different concentrations were added and the cells were further incubated for 30 min, subsequently exposed to an NIR laser (808 nm, 1.5 W/cm^2) for 10 min, and then incubated for another 24 h. After that the Alamar Blue (Invitrogen) assay were performed to evaluate the viability of 4T1 and EC cells.

2.11. In vivo thermal imaging of microspheres

Infrared thermal image was used to investigate the photothermal effect of PDA@PLGA microspheres in mice. For photothermal imaging, female BALB/c mice with a 4T1 tumor of 50 mm^3 on the back were intratumorally injected with PBS, PDA@PLGA and PDA/DOX·HCl@PLGA, respectively. Firstly, the mice were anesthetized with 2 wt% sodium pentobarbital solution. The volume of solution injected was 100 μL for each mouse. The concentrations in the microsphere group were the same, while the free DOX·HCl group was maintained an equivalent dose of 5 mg/kg and the PDA content was maintained an equivalent dose of 4 mg/mL for all PDA-containing groups. Thereafter, infrared thermal imaging was performed on the mice with an infrared laser irradiation (808 nm, 1.5 W/cm^2) for 10 min and at intervals of 2 min. The images were analyzed using the infrared camera software SmartView.

2.12. Drug distribution in vivo

For *in vivo* fluorescent imaging, BALB/c mice with a 4T1 tumor of 50 mm^3 on the back were randomized into four groups. PDA/DOX·HCl@PLGA and DOX·HCl were injected intratumorally. Free DOX·HCl was injected intravenously. The free DOX·HCl group was maintained an equivalent dose of 5 mg/kg. The mice were monitored with *in vivo* fluorescent imaging system (CRi Maestro, USA) at preset time points (6, 24, 72, and 168 h postinjection). After 168 h, the mice were euthanized, and the tumor and main organs were harvested and imaged. For PDA/DOX·HCl@PLGA, treatment of irradiation and non-irradiation were both applied and the mice from irradiation group were irradiated with NIR laser 808 (1.5 W/cm^2) for 10 min at 0, 48 and 96 h postinjection.

To further quantitatively evaluate the biodistribution of the DOX·HCl, tumor-bearing mice from different groups (intravenously DOX·HCl group, intratumorally DOX·HCl group, intratumorally PDA/DOX·HCl@PLGA group with or without light irradiation) after treatment as previously described were also sacrificed at the indicated time intervals (6 h, 24 h, 72 h and 168 h). Normal organs (liver, heart, spleen, lung, and kidney) and tumor tissue were collected from the mice. Tissue samples were washed in PBS, wiped with filter paper, weighed and then stored at −20 °C until undergoing analysis. The fluorescence of the samples was measured. The tissue distribution of DOX·HCl was expressed as the amount of DOX·HCl per gram of tissue.

2.13. In vivo antitumor activity

About 2×10^5 4T1 cells suspended in 100 μL of serum free cell medium were inoculated subcutaneously in female BABL/c mice. The mice were used for further experiments when the tumor volume of the mice was approximately 50 mm^3. Tumor-bearing mice were randomized into seven groups and were injected intravenously or intratumorally with PBS, DOX·HCl, PDA@PLGA and PDA/DOX·HCl@PLGA. Dosage for free DOX·HCl group was 5 mg/kg. PDA dosage was 4 mg/mL for all PDA-containing groups. For the laser irradiation treatment groups, after 0, 2, 4 day injection, the mice were irradiated by the 808 nm laser at the power density of 1.5 W/cm^2 for 10 min. The tumor volume was measured by a caliper and calculated as $V = (a \times b^2)/2$, where “a” and “b” are the longest and shortest diameters, respectively. It is worth noting that the measurement of tumor volume in mice were started from day 0 (when the initial treatment were performed), then measured and recorded every 2 days until the 21st day. Measurements of mice body weights were also started on day 0, then measured and recorded every 2 days until the 21st day. The survival rates were recorded every 2 days from day 0 to day 42. After

21 days treatment, one mouse was randomly selected from each group and photographed. The organs (e.g. heart, liver, spleen, lung and kidney) and tumor tissues were collected and further used for histology analysis. Tissue sections of organs and tumors with thickness of 5 μm were stained with hematoxylin/eosin (H&E). The tumor tissue sections were also detected with the In Situ Cell Death Detection Kit (Roche Diagnostics GmbH, Mannheim, Germany) for terminal deoxynucleotidyl transferase dUTP nick-end labeling (TUNEL) assay, or immunostained with a rabbit polyclonal antibody for Ki-67 (Abcam, Cambridge). The stained tissues were observed and imaged by an optical microscope (BA210, Motic, China). In addition, the weights of the tumor tissues of mice from different groups were recorded when the mice dead.

2.14. Western blot

After 21 days of treatment, the obtained tumor tissue were also used for Western Blot. For western blot, the tumor tissues were lysed on ice with RIPA lysis buffer, and then centrifuged at 9800 × *g* for 20 min to collect the supernatant. Proteins were recovered and separated by sodium dodecyl sulfate-polyacrylamide gel electrophoresis. After that, proteins were transferred to a PVDF membrane and blocked with 5% fat-free milk. The primary antibodies (dilution) were incubated overnight at 4 °C, including Hsp70 (abcam), Bax (abcam), Bcl-2 (abcam) or β-actin (abcam), followed by secondary antibody incubation. Finally the proteins were detected using ECL reagent according to the manufacturer's instructions.

2.15. Statistical analysis

Unless otherwise specified in this experiment, all experiments were set up at least 3 parallel groups, and the data were expressed as mean ± standard deviation (mean ± SD). One way ANOVA was performed to determine statistical significance of the data. When $0.05 < p$, there was no significant difference, represented by symbol #. When $0.01 < p < 0.05$, there was a significant difference, represented by the symbol *; when $p < 0.01$, the difference is extremely significant, represented by the symbol **.

3. Results and discussion

3.1. The optimization of coaxial electrospraying process

To maintain a stable electrospraying process and obtain well-defined hollow microspheres, the process parameters of electrospraying, including polymer concentration, external flow rate, receiving distance and voltage, were optimized. Samples were characterized by scanning electron microscopy (SEM), and the size of the microspheres was statistically analyzed using ImageJ software. The polydispersity of the microspheres was also evaluated. As the SEM images in Figs. 1A1–A3 and S1A1–A3 show, the morphologies of the microspheres displayed disc-shapes to spherical shapes and beaded fibers as the PLGA concentration increased to 10 wt%, 20 wt%, and 30 wt%, respectively. To obtain the well-defined microspheres in the following experiment, the PLGA concentration was fixed at 20 wt%. Then, the flow rate of the external phase, collecting distance and voltage were also optimized in this order. Figs. 1B1–B4, S1B1–B3 and Table S1 in the Supplementary Material (SM) show that all microspheres had a good spherical morphology with an average diameter of 5.0 μm when changing the flow rate of the external phase from 0.6 mL/h to 1.0 mL/h. The relative standard deviation (RSD) of the microsphere size was utilized to demonstrate the uniformity of the microspheres [56,57,60]. We find that when the flow rate of the external phase was 0.8 mL/h, the RSD value was only 10%, suggesting that the microspheres had a uniform size. Thus, 0.8 mL/h was fixed as the flow rate of the external phase for the followed optimized experiments. The other factors were fixed, and only the collecting distance was changed to 20 cm. The corresponding RSD value is 10.6% (Fig. 1C1–C4, Fig. S1C1–C3 and Table S1). Similarly, when the voltage was 12 kV, the RSD was the smallest, at only 9.9% (Figs. 1D1–D4 and S1D1–D3). Taken together, the optimized conditions for the fabrication of size uniform microspheres are a polymer concentration of 20 wt%, an external phase flow rate of 0.8 mL/h, a collecting distance of 20 cm and a voltage of 12 kV. Under these conditions, the microspheres with a diameter of 5.32 ± 0.05 μm and RSD of 9.9% were harvested.

3.2. Characterization of the hollow structured microspheres

To confirm the hollow structure of the microspheres, transmission electron microscopy (TEM), cryo-scanning electron microscopy (cryo-SEM) and confocal laser scanning microscopy (CLSM) were used. First, both the individual PDA nanoparticles and hollow structured microspheres containing PDA nanoparticles were characterized by TEM. From the TEM images shown in Fig. 2A and B, the PDA nanoparticles with a size of approximately 350 nm were spherical and were successfully encapsulated in the interior hollow spaces of the microspheres as indicated by the yellow arrows. Furthermore, from the cryo-SEM images of the cross-sectionals view of the microsphere in Fig. 2C and D, we can also clearly see the hollow space and PDA nanoparticles (indicated by yellow arrows) were encapsulated in the space, with a shell layer of approximately 1 μm in thickness (indicated by red arrows). In addition, to further confirm the hollow structure of the microspheres, Nile red dye was encapsulated in the PLGA shell layers. From the CLSM observation in Fig. 2E, we can clearly see the size uniform red circles with black cores. Together, these results demonstrated that the microspheres fabricated using the coaxial electrospraying technique possess a hollow structure and that the PDA nanoparticles can be successfully encapsulated in the hollow space. Accordingly, both the PDA nanoparticles and the anticancer drug, DOX·HCl, exhibiting red fluorescence, were encapsulated into the hollow structured microspheres (PDA/DOX·HCl@PLGA). From the CLSM image in Fig. 2F, the microspheres with spherical red cores and light red shells can be seen, suggesting that the DOX.HCl can be encapsulated into the hollow spaces of the microspheres. The loading content (LC) and encapsulation efficiency (EE) of DOX·HCl in the microspheres were ~1% and ~90.3%, respectively.

3.3. Photothermal properties of PDA nanoparticle loaded microspheres

To characterize the photothermal conversion efficiency, an infrared thermal camera was used to monitor the microspheres in water under a constant NIR irradiation (808 nm, 1.5 W/cm^2). The infrared thermal images are shown in Fig. 3A, and the corresponding heating curves are shown in Fig. 3B. The results show that with an increasing concentration of the microspheres, the temperature of the solutions gradually increased over 10 min, whereas there was no change in the temperature of the deionized water group. The increases of the emulsion temperature (ΔT) after irradiation (808 nm, 1.5 W/cm^2) for 10 min were obtained for all samples as follows: ~2.5 °C for pure water, ~12 °C, ~20 °C, ~25 °C and ~ 32 °C for the microspheres solutions at concentrations of 1 mg/mL, 2 mg/mL, 4 mg/mL and 8 mg/mL, respectively (Fig. 3B). The temperature can be enhanced to more than 50 °C in the irradiation region, which is sufficiently high for killing the cells due to the hyperthermia reported previously [6]; therefore, the microsphere concentration of 4 mg/mL was selected for the followed investigations, including the animal experiments.

The effect of laser intensity on the temperature of the 4 mg/mL microsphere dispersing solution with was further investigated as shown in Fig. 3C. After irradiation for 10 min, the ΔT reached 10 °C (0.5 W/cm^2), 15 °C (1.0 W/cm^2), 25 °C (1.5 W/cm^2) and 27.5 °C (2.0 W/cm^2), suggesting that the increase of the temperature of the solution became faster with increasing laser intensity. Thus, the laser intensity of 1.5 W/cm^2 was fixed for the following experiments.

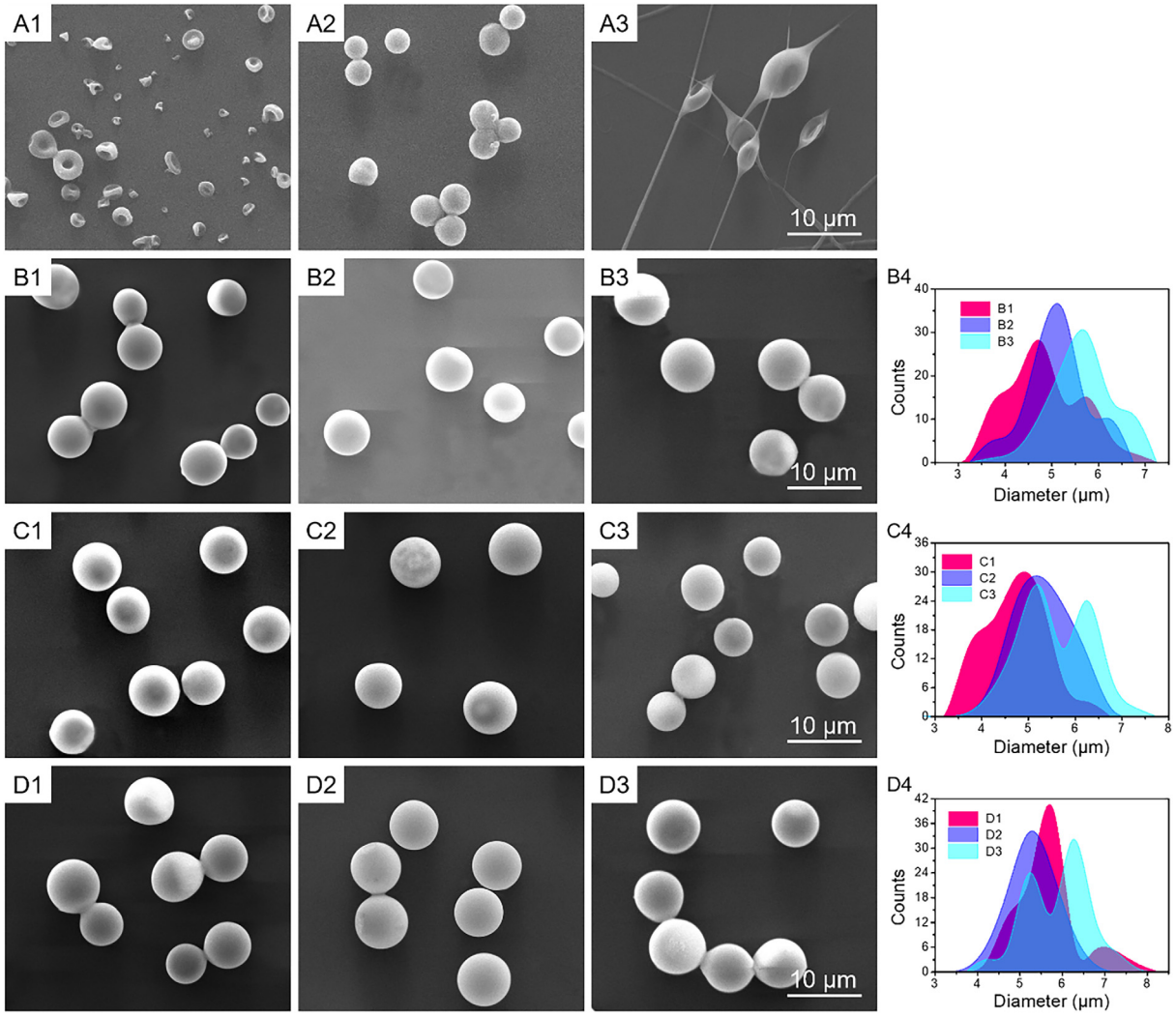

Fig. 1. The optimization of the coaxial electrospraying process for preparing microspheres. A1–A3) The polymer concentrations: 10 wt%, 20 wt% and 30 wt%. B1–B3) The external phase flow rates: 0.6 mL/h, 0.8 mL/h and 1.0 mL/h. C1-C3) The receiving distance: 15 cm, 20 cm and 25 cm. D1–D3) The voltages: 10 kV, 12 kV and 14 kV. B4, C4 and D4 were the corresponding particle size distributions, respectively.

Additionally, the photostability of the microspheres was also evaluated. The solutions at 4 mg/mL were irradiated by the 808 nm NIR laser (1.5 W/cm^2) for 5 min (laser on), followed by cooling to room temperature (10 min, laser off). This cycle was repeated five times and the corresponding variations of ΔT were recorded (Fig. 3D), which demonstrated that the ΔT was maintained at approximately 23 °C. The absorbance of the irradiated samples under different irradiation times were also investigated and no obvious changes were found (Fig. 3E). These results indicated that PDA@PLGA microspheres have high photostability under NIR laser irradiation, such that PDA-loaded microspheres possess high photothermal conversion efficiency and high photostability, and may be a potential anticancer therapeutic agent for photothermal therapy.

3.4. *In vitro* drug release

The *in vitro* DOX·HCl release behaviors from PDA/DOX·HCl@PLGA microspheres were investigated as shown in Fig. 3F and G. Phosphate buffer saline (PBS) at pH 6.8 was used as the release medium to mimic the slightly acidic tumor environment [61]. For the nonirradiation group (PDA/DOX·HCl@PLGA-light) and the group (PDA/DOX·HCl@PLGA + light) irradiated with NIR laser (808 nm, 1.5 W/cm^2) at intervals of 48 h, there was an obvious burst release with a release amount of ~35% within the first 24 h. The irradiation group and nonirradiation group showed the same trend in release profiles, and the former had a cumulative release amount of over 80% in 21 days, which was approximately 10% higher than that of the latter because the laser irradiation was applied every other day beginning at day 2 (Fig. 3F and G).

To explore the mechanism by which laser irradiation regulates drug release behavior, SEM was used to observe the *in vitro* degradation of PDA/DOX·HCl@PLGA microspheres over 7 days with/without laser irradiation. From the SEM images in Fig. S2 in the Supplementary Material (SM), when irradiation is applied, holes began to occur on the surface of some microspheres and the interior hollow spaces were gradually exposed at day 3. Additionally, the number of microspheres with holes increased, and the holes became larger after 7 days. However, in the nonirradiation group, during the first 3 days, the microspheres were mainly unchanged, although at 7 days, holes on some of the microspheres occurred. The drug release of PLGA microspheres primarily includes two mechanisms: the diffusion of drug molecules and degradation of the polymer matrix [62]. The faster the degradation, the faster the drug release. The degradation of PLGA is the hydrolysis of ester bonds in the polymer backbone, which can be accelerated by heating. At the same time, the heat generated by the photothermal effect could also promote the diffusion of drug, contributing to the increase of drug release.

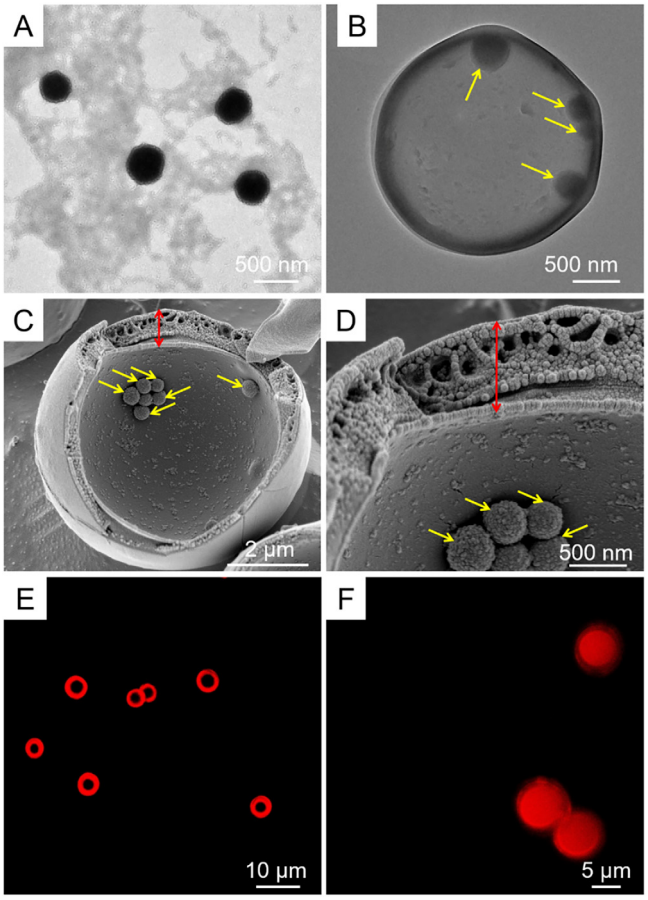

Fig. 2. Morphologies of PDA nanoparticles and PDA@PLGA microspheres. A) TEM images of PDA nanoparticles. B) TEM image of PDA@PLGA microspheres. C, D) Cryo-SEM image of PDA@PLGA microspheres. The yellow arrows indicate PDA nanoparticles and the red arrows stand for the cross section of the shell part of the hollow microsphere. E) CLSM image of PDA@PLGA microsphere, and the PLGA shell stained with Nile red. F) CLSM image of PDA/DOX•HCl@PLGA microspheres.

3.5. In vitro antitumor effect

The cytotoxicity of the blank PDA@PLGA microspheres and *in vitro* antitumor effect of PDA/DOX·HCl@PLGA with/without laser irradiation were investigated by coculture with either endothelial cells (ECs) or a mouse mammary tumor cell line (4T1 cells). From the fluorescent images of live/dead staining shown in Fig. 4A, without laser irradiation and with an increase of the microsphere concentration, both ECs and 4T1 cells were alive and grew healthily. From the Alamar blue assay in Fig. 4B, the viabilities of both ECs and 4T1 cells were remained over 90% when the concentration of microspheres reached 8 mg/mL, indicating that the PDA@PLGA microspheres had good cytocompatibility during nonirradiation. However, when laser irradiation was applied, the photothermal cytotoxicity of PDA@PLGA occurred. In the fluorescent images of Fig. 4C, the number of dead ECs and 4T1 cells increased with an increase of the microsphere concentration due to laser irradiation. Furthermore, only a few cells survived when the concentration of microspheres reached 8 mg/mL for both cell lines (Fig. 4C and D).

Next, the *in vitro* antitumor effect of PDA/DOX·HCl@PLGA microspheres containing both PDA nanoparticles and DOX·HCl was evaluated with 4T1 cells under the conditions of irradiation and nonirradiation. In Fig. 4E, when the concentration of microspheres increased to 4 mg/mL, most cells were dead under irradiation, and the cell viability was only ~30% (Fig. 4F). However, few dead cells were found in the nonirradiation group. These results demonstrated that the photothermal cytotoxicity of PDA/DOX·HCl@PLGA microspheres is much better than the cytotoxicity of chemotherapeutic drugs for cancer therapy.

3.6. In vivo thermal imaging of microspheres

The *in vivo* photothermal effect of microspheres was investigated in 4T1 tumor-bearing mice. As shown in Fig. 5, after 10 min irradiation with the NIR laser (808 nm, 1.5 W/cm^2), the temperature of the tumor site in the PBS group was not significantly elevated, indicating that NIR laser irradiation alone could not generate adequate heat *in vivo* without the help of photothermal conversion materials. For the PDA@PLGA + Laser group, the temperature at the tumor site gradually increased to ~60 °C with irradiation time, indicating a clear *in vivo* photothermal effect. For the PDA/DOX·HCl@PLGA + Laser group, after 10 min of NIR laser irradiation, the temperature of the tumor site also rose to ~60 °C, indicating that the loading of DOX·HCl did not affect the photothermal conversion effect of the microspheres and is suitable for photothermal therapy.

3.7. Drug distribution in vivo

To visualize the distribution of DOX·HCl *in vivo*, the PDA/DOX·HCl@PLGA and free DOX·HCl solutions were intratumorally injected into 4T1 tumor-bearing Balb/C mice, with the free DOX·HCl solution and saline intravenously injected as controls. An equivalent DOX·HCl dose of 5 mg/kg body weight was applied for the DOX-containing groups. The mice in the PDA/DOX·HCl@PLGA + Laser group were irradiated with NIR laser (808 nm, 1.5 W/cm^2) for 10 min at 0, 48 and 96 h postinjection. From the *in vivo* fluorescence images shown in Fig. 6a, clear DOX fluorescence was seen around the tumor site from these groups of DOX·HCl (intratumorally) and PDA/DOX·HCl@PLGA with (+Laser)/without laser irradiation (−Laser) after 6 h. As expected, the strong fluorescence intensity in mice from the PDA/DOX·HCl@PLGA + Laser and PDA/DOX·HCl@PLGA-Laser groups was always maintained because the DOX·HCl encapsulated in the microspheres was gradually released with time. However, the fluorescence intensity in mice from the DOX·HCl (intratumorally and intravenously) groups decreased and little fluorescence was observed in the intravenous injection DOX·HCl group at 6 h, indicating that the free DOX·HCl, a small molecule drug, can easily diffuse into other tissues and be cleared from the body.

At 168 h postadministration, mice were sacrificed, and normal organs (e.g., liver, heart, spleen, lung, and kidney) and tumor were harvested to observe the DOX fluorescence distribution. Clear DOX fluorescence was found in the tumor tissues, and almost no fluorescence was found in other organs for the PDA/DOX·HCl@PLGA groups, with or without laser irradiation. In the DOX·HCl (intratumorally) group, weak drug fluorescence was distributed both in the tumor and liver, suggesting that local intratumoral drug administration helped increase local drug enrichment in tumor that and free drug continued to diffuse into other organs.

To further quantitatively confirm the DOX·HCl distribution *in vivo*, the amount of accumulated DOX in the tumors and major tissues of tumor-bearing Balb/C mice was tested with a fluorescence spectrophotometer at 6, 24, 72 and 168 h postadministration. An equivalent DOX·HCl dose of 5 mg/kg body weight was used, and the dose was administered only once for all the groups. In Fig. 6B, the DOX·HCl levels are the highest in the tumor tissues in all intratumoral injection groups. In particular, the PDA/DOX·HCl@PLGA microspheres show the cumulative content of DOX·HCl of more than 22% in the tumor at 6 h, which is approximately 6-fold higher than that (~4%) of the intravenous injection DOX·HCl group. Furthermore, in the laser irradiation group, the cumulative content of DOX·HCl in tumor is slightly higher than the group without irradiation, which is mainly due to the release of DOX·HCl because of the photothermal effect. The accumulated amount

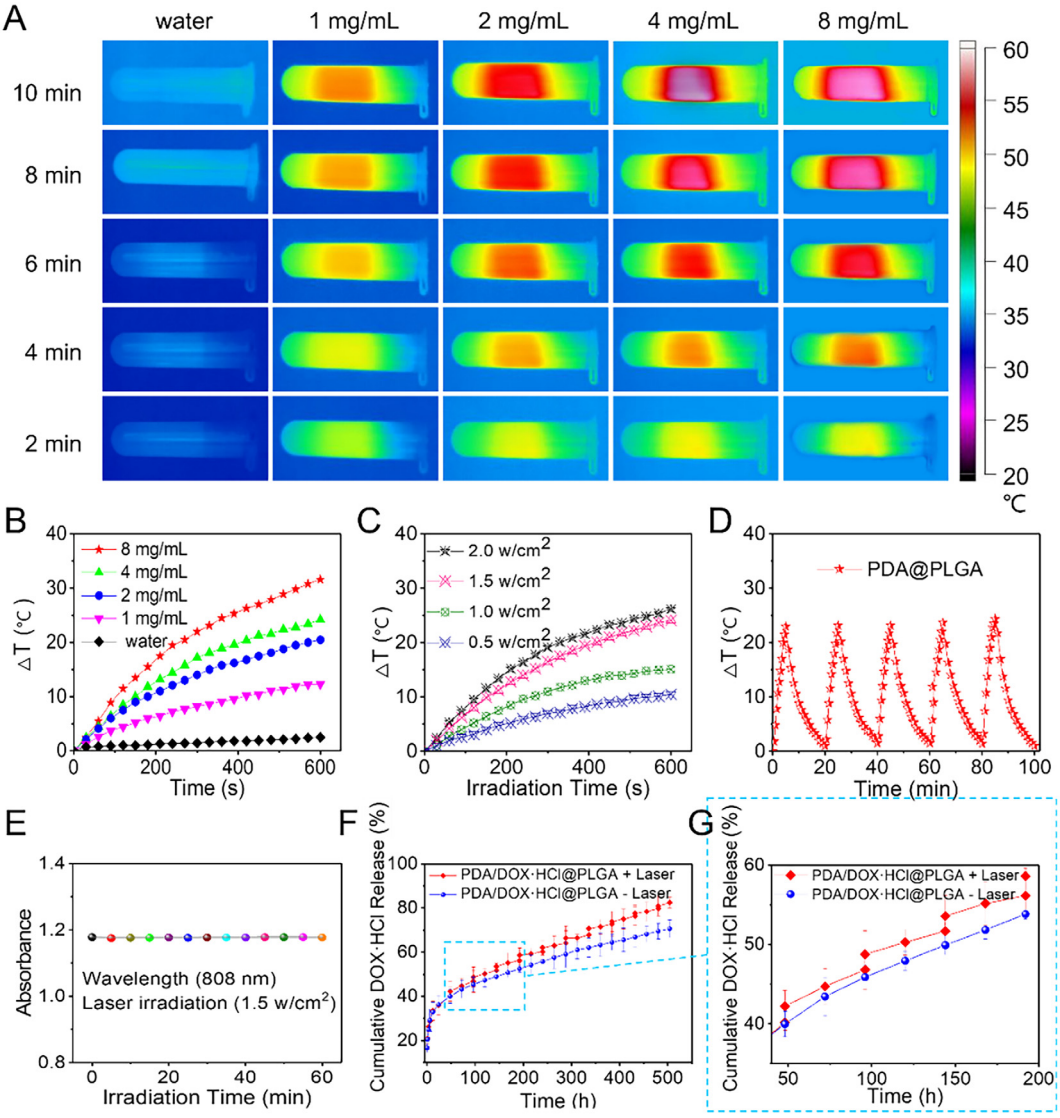

Fig. 3. Photothermal properties of PDA nanoparticle loaded microspheres. A, B) The infrared thermal images of water and PDA@PLGA microsphere aqueous solutions at different concentrations (1 mg/mL, 2 mg/mL, 4 mg/mL and 8 mg/mL), which were irradiated with the 808-nm laser (1.5 W/cm^2). C) Heating curves of the PDA@PLGA microsphere aqueous solution at 4 mg/mL irradiated with the 808-nm laser at the power densities of 0.5 W/cm^2, 1.0 W/cm^2, 1.5 W/cm^2 and 2.0 W/cm^2. D) Temperature change of the PDA@PLGA microsphere solution at 4 mg/mL over five laser on/off cycles (808 nm, 1.5 W/cm^2). E) UV absorbance at 808 nm versus the irradiation time. F, G) NIR-triggered release of DOX·HCl from PDA/DOX·HCl@PLGA microspheres, which were irradiated with an 808 nm NIR laser (1.5 W/cm^2).

in the tumor is also much higher than the intravenous injection of other nanomedicines [63,64]. Additionally, the content of DOX·HCl in the normal tissues is lower than in the tumors for all intratumoral injection groups, which is different from the intravenous injection of other nanomedicines reported previously. The result also suggested that the intratumoral injection of microspheres can decrease the side effects of anticancer drugs to normal tissues. With increasing time, the content of DOX·HCl in tumors gradually decreased in all groups due to the metabolism of the free drug; however, at 168 h postinjection, the content in tumors remained ~10% for the intratumoral injection microspheres groups. The high drug enrichment in the tumor is of great importance for enhanced chemotherapy efficiency. Therefore, local drug delivery could significantly enhance the content of drug in the tumor tissue and maintain high drug enrichment in the tumor over time, which contributed to an increase of therapeutic efficacy against the tumor and a reduction of the side effects to normal tissues.

3.8. *In vivo* antitumor activity

The *in vivo* antitumor activities of different drug formulations were investigated on 4T1 tumor-bearing Balb/C mice. Changes of tumor volume in mice from different groups were recorded over 21 days of treatment every two days beginning at the first treatment as shown in Fig. 7A–C. The tumor growth of mice in the PDA/DOX·HCl@PLGA + Laser group was the slowest, and the relative average tumor volume at day 21 was only 1.4 due to the synergistic effect of the photothermal therapy and chemotherapy. Furthermore, the relative mean tumor volume in the PDA/DOX·HCl@PLGA–Laser group was ~4.0, higher than the (~2.8) in the PDA@PLGA + Laser group without anticancer drug, suggesting that photothermal therapy plays a dominant role in the local chemo-photothermal combination therapy. The body weight of the mice gradually increased over 21 days and there was no significant difference among all groups (Fig. 7D). The survival rates of mice in these groups at 42 days were significantly different (Fig. 7E). The PDA@PLGA + Laser and PDA/DOX·HCl@PLGA + Laser groups,

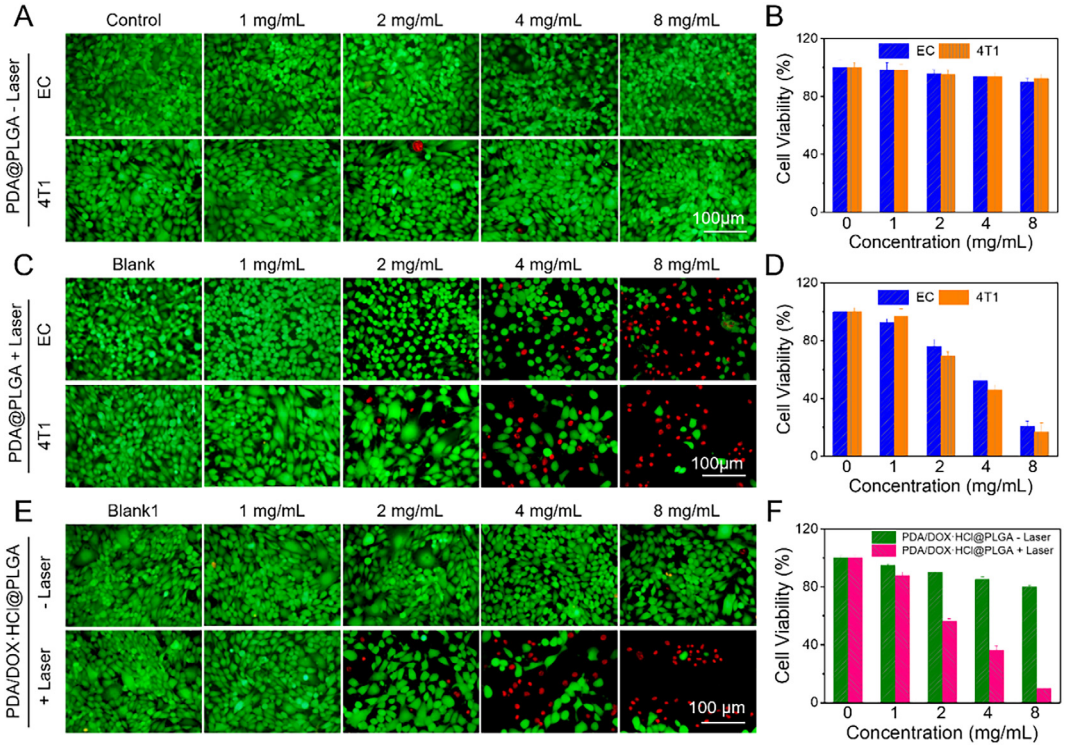

Fig. 4. *In vitro* cell viability of EC and 4T1 cells. A) Fluorescence images showing the viability of EC and 4T1 cells following treatment with different concentrations of PDA@PLGA microspheres (without NIR laser irradiation) for 24 h. Green calcein AM fluorescence and red PI fluorescence indicating live and dead cells, respectively. B) EC and 4T1 cells incubated with different concentrations of PDA@PLGA microspheres (without NIR laser irradiation) for 24 h. C) The fluorescence images ECs and 4T1 cells treated with different concentrations PDA@PLGA microspheres stained with calcein AM (green, live cells) and propidium iodide (red, dead cells) after irradiation with the 808-nm laser at the power density of 1.5 W/cm^2. D) *In vitro* cell viabilities of ECs and 4T1 cells incubated with various concentrations of PDA@PLGA microspheres with 808 nm NIR laser irradiation (1.5 W/cm^2). E) The fluorescence images of 4T1 cells treated with different concentrations of PDA/DOX·HCl@PLGA microspheres (with and without NIR Laser irradiation) stained with calcein AM (green, live cells) and propidium iodide (red, dead cells). F) *In vitro* cell viabilities of 4 T1 cells incubated with various concentrations of PDA/DOX·HCl@PLGA microspheres with and without 808 nm NIR laser irradiation (1.5 W/cm^2). (For interpretation of the references to colour in this figure legend, the reader is referred to the web version of this article.)

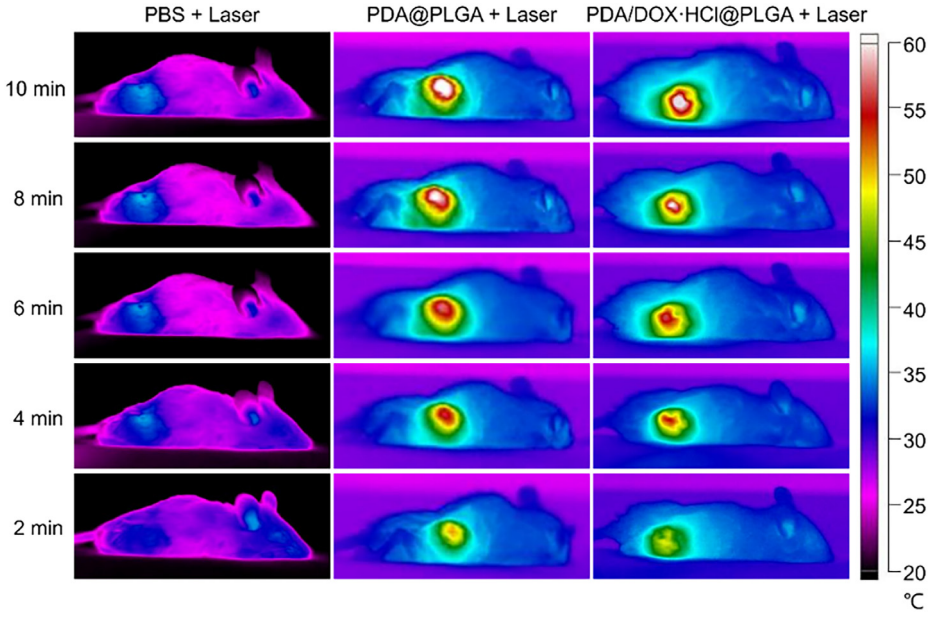

Fig. 5. Infrared thermal images of 4T1 tumor-bearing mice intratumorally injected with PBS, PDA@PLGA and PDA/DOX·HCl@PLGA with NIR laser irradiation (1.5 W/cm^2) for 10 min.

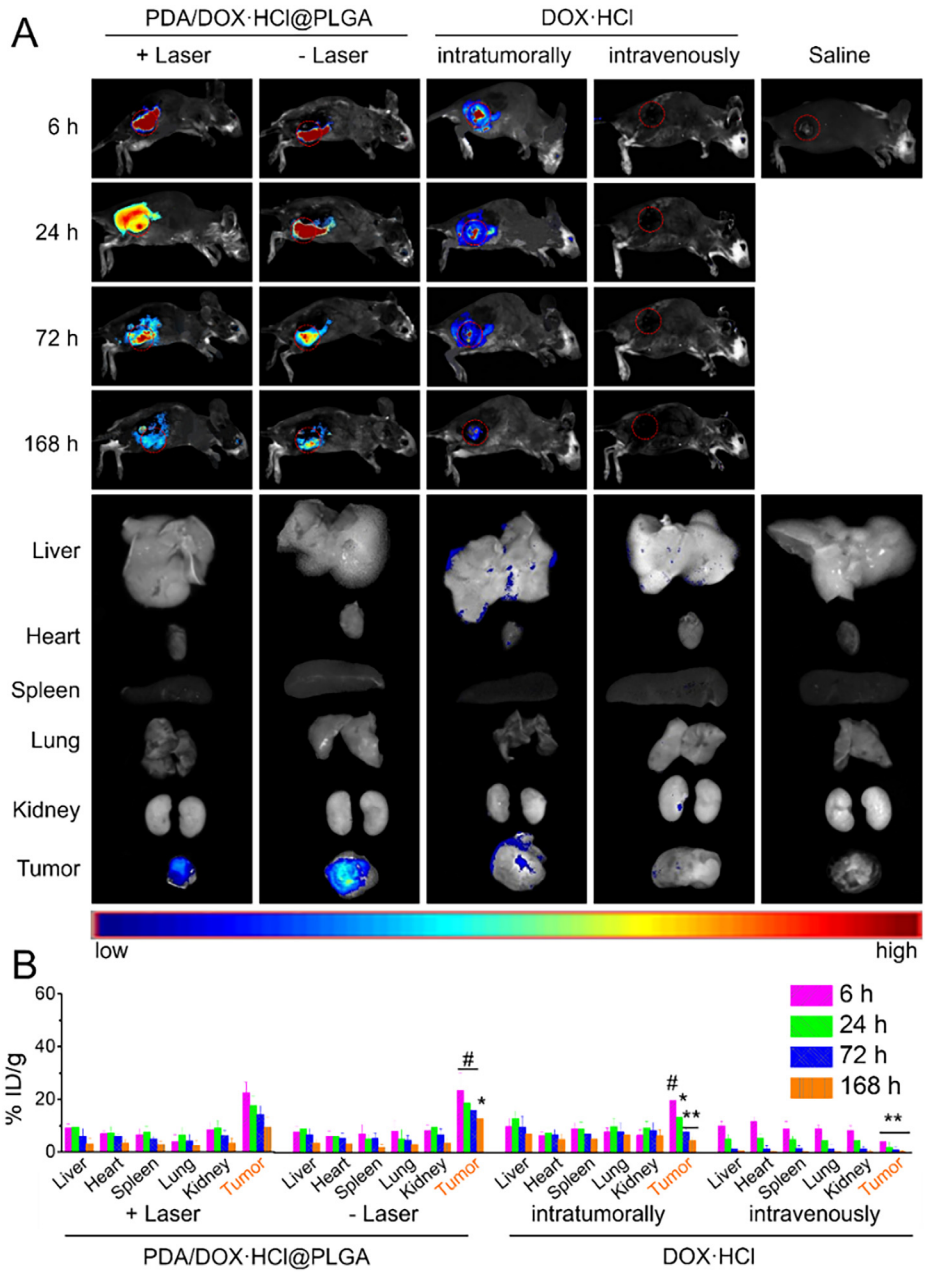

Fig. 6. DOX·HCl biodistribution. A) In vivo and ex vivo DOX·HCl fluorescence images showing the DOX·HCl biodistribution in 4T1 tumor bearing mice after intratumoral (PDA/DOX·HCl@PLGA, DOX·HCl and PBS) or intravenous (DOX·HCl) injection for different time periods. B) Drug biodistribution in normal tissues (liver, heart, spleen, lung, and kidney) and tumor tissues after intratumoral (PDA/DOX·HCl@PLGA and DOX·HCl) or intravenous (DOX·HCl) injection for different time periods. The + Laser group was irradiated with NIR laser 808 nm (1.5 W/cm^2) for 10 min at 0, 2 and 4 days. ($^*p < 0.05$, $^{**}p < 0.01$ and $\#p > 0.05$ compared with the PDA/DOX·HCl@PLGA + Laser group at the corresponding time point).

which were irradiated with NIR laser at 808 nm (1.5 W/cm^2, 10 min), had survival rates of 85.71% and 100%, respectively, at the 42nd day, suggesting that photothermal therapy significant inhibits tumor growth and there was extremely low toxicity to normal tissues. For the combination of photothermal therapy with chemotherapy in the PDA/DOX·HCl@PLGA + Laser group, the highest survival rate (100%) was obtained due to the synergistic effect. The intravenous injection of free DOX·HCl displays a low survival rate (14.29%), indicating its serious systematic toxicity and low therapeutic efficacy because of its distribution throughout the body.

To further evaluate the antitumor activity, histological (hematoxylin/eosin (H&E) and *in situ* terminal deoxynucleotidyltransferase mediated UTP end labeling (TUNEL)) and immunohistochemical analyses were applied to tumor tissues from different group, as shown in Fig. 7F. From the H&E staining images, almost no apoptotic tumor cells were found in the PBS + Laser and PDA@PLGA-Laser groups, indicating that the treatments with a single laser irradiation or single hyperthermia agent could not induce cell apoptosis, whereas the tumor cells in the other groups showed different degrees of apoptosis, particularly for the PDA/DOX.HCl@PLGA + Laser group, which mainly manifested as necrosis of the tumor tissue, reduced cell tightness, incomplete cell membrane structure and nuclear lysis. Similarly, the TUNEL staining results also demonstrated that the PDA/DOX.HCl@PLGA + Laser group exhibited remarkable antitumor effects, as evidenced by the largest area of apoptotic cells identified in brown. In addition, an immunohistochemical analysis was performed to evaluate the expression of Ki67 protein (a biomarker of cell proliferation). The Ki67 level in the PDA/DOX·HCl@PLGA + Laser group was the lowest, and a large area of cells was stained blue, indicating that the local combination of photothermal therapy and chemotherapy suppressed tumor cell proliferation and promoted antitumor activity.

Finally, we investigated the anticancer mechanism of the synergism between photothermal therapy and chemotherapy at the protein level by western blot analysis of heat shock protein 70 (Hsp70), Bcl-2 protein and Bax protein. The Hsp70 protein is synthesized in response to heat stress to protect the cell from thermal damage [65]. In Fig. 7G and I,

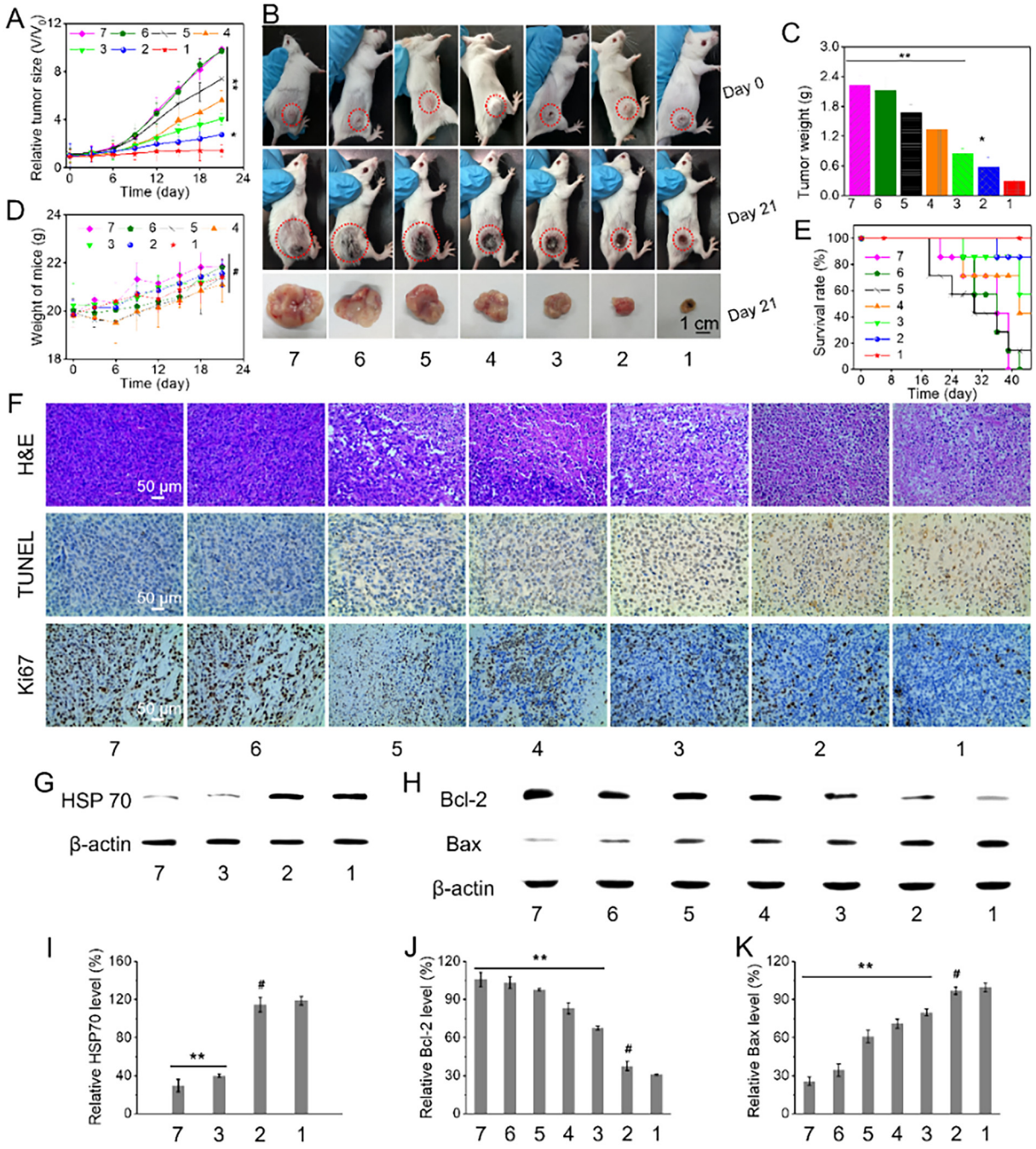

Fig. 7. In vivo antitumor effect. A) Relative tumor size. B) Photos of 4T1 tumor bearing mice and excised 4T1 solid tumors from different treatment groups at day 21. C) The weight of tumor tissues. D) Body weight changes. E) Survival rate curves. F) H&E, TUNEL and Ki67 protein analysis of tumor tissues of female mice at day 21 after treatment with various formulations. G, H) Representative heat shock protein 70 (HSP70), Bcl-2 and Bax were analyzed by western blot. (7 = PBS + Laser, 6 = PDA@PLGA − Laser; 5 = DOX·HCl (intravenously); 4 = DOX·HCl (intratumorally); 3 = PDA/DOX·HCl@PLGA - Laser; 2 = PDA@PLGA + Laser; 1 = PDA/DOX·HCl@PLGA + Laser) ($^{*}p < 0.05$, $^{**}p < 0.01$ and $\#p > 0.05$ compared with the PDA/DOX·HCl@PLGA + Laser group at the corresponding time point).

compared with the PBS + Laser and PDA/DOX·HCl@PLGA-Laser groups, the expression of Hsp70 was significantly increased ~3 fold after NIR laser irradiation, indicating that with PDA-containing microspheres, NIR laser irradiation could successfully induce hyperthermia to inhibit tumor growth. The apoptosis-related proteins, Bcl-2 and Bax, were also analyzed by western blot (Fig. 7H, J, K). The mice treated with PDA@PLGA + Laser or PDA/DOX·HCl@PLGA + Laser exhibited a significant downregulation of Bcl-2 and upregulation of Bax. These results further demonstrated that the local combination of photothermotherapy and chemotherapy could significantly induce tumor cell apoptosis.

4. Conclusion

In summary, we developed a hollow structured biodegradable microsphere containing both PDA nanoparticles and DOX·HCl in the hollow space *via* a coaxial electrospraying method. These uniformly sized microspheres possess high photothermal conversion efficiency and high photostability. When laser irradiation is applied, degradation of the polymer shell of the microsphere as accelerated due to the heat generated by the photothermal effect, further promoting the release of DOX·HCl. In contrast to traditional intravenously injected nanomedicines, an extremely high content of DOX·HCl in the tumor was achieved,

with over 22% at 6 h and ~10% at 168 h after intratumoral injection of the microspheres. With NIR laser irradiation at the tumor site of tumor-bearing mice, a 100% survival rate and significant tumor growth inhibition was achieved. Local drug delivery could ensure both a high drug dose and hyperthermia at the tumor site, thereby initiating cell apoptosis. The local chemo-photothermal combination therapy significantly enhanced the therapeutic efficacy against a solid tumor and simultaneously reduced the side effects to normal tissues, and has great potential for development as a new strategy for clinical cancer therapy.

Acknowledgments

This work was partially supported by the China National Funds for Distinguished Young Scientists (No. 51725303), National Natural Science Foundation of China (Nos. 21574105, 51703189), the Sichuan Province Youth Science and Technology Innovation Team, China (Grant No. 2016TD0026) and the Fundamental Research Funds for the Central Universities, China (No. 2682017CX040).

Appendix A. Supplementary data

Supplementary data to this article can be found online at https://doi.org/10.1016/j.cej.2019.122317.

References

[1] A.I. Minchinton, I.F. Tannock, Drug penetration in solid tumours, Nat. Rev. Cancer 6 (2006) 583–592.
[2] C. O'Gorman, W. Sasiadek, S. Denieffe, M. Gooney, Predicting radiotherapy-related clinical toxicities in cancer: a literature review, Clin. J. Oncol. Nurs. 18 (2014) E37–E44.
[3] Q. Tian, M. Tang, Y. Sun, R. Zou, Z. Chen, M. Zhu, S. Yang, J. Wang, J. Wang, J. Hu, Hydrophilic flower-like cus superstructures as an efficient 980 nm laser-driven photothermal agent for ablation of cancer cells, Adv. Mater. 23 (2011) 3542–3547.
[4] X. Zhu, W. Feng, J. Chang, Y.W. Tan, J. Li, M. Chen, Y. Sun, F. Li, Temperature-feedback upconversion nanocomposite for accurate photothermal therapy at facile temperature, Nat. Commun. 7 (2016) 10437.
[5] S. Lal, S.E. Clare, N.J. Halas, Nanoshell-enabled photothermal cancer therapy: Impending clinical impact, Acc. Chem. Res. 41 (2008) 1842–1851.
[6] Y. Liu, K. Ai, J. Liu, M. Deng, Y. He, L. Lu, Dopamine-melanin colloidal nanospheres: an efficient near-infrared photothermal therapeutic agent for in vivo cancer therapy, Adv. Mater. 25 (2013) 1353–1359.
[7] Y. Wang, G. Wei, X. Zhang, X. Huang, J. Zhao, X. Guo, S. Zhou, Multistage targeting strategy using magnetic composite nanoparticles for synergism of photothermal therapy and chemotherapy, Small 14 (2018) e1702994.
[8] W.I. Choi, J.Y. Kim, C. Kang, C.C. Byeon, Y.H. Kim, G. Tae, Tumor regression in vivo by photothermal therapy based on gold-nanorod-loaded, functional nanocarriers, ACS Nano 5 (2011) 1995–2003.
[9] H. Liu, D. Chen, L. Li, T. Liu, L. Tan, X. Wu, F. Tang, Multifunctional gold nanoshells on silica nanorattles: a platform for the combination of photothermal therapy and chemotherapy with low systemic toxicity, Angew. Chem. Int. Ed. Engl. 50 (2011) 891–895.
[10] M.S. Noh, S. Lee, H. Kang, J.K. Yang, H. Lee, D. Hwang, J.W. Lee, S. Jeong, Y. Jang, B.H. Jun, D.H. Jeong, S.K. Kim, Y.S. Lee, M.H. Cho, Target-specific near-ir induced drug release and photothermal therapy with accumulated au/ag hollow nanoshells on pulmonary cancer cell membranes, Biomaterials 45 (2015) 81–92.
[11] A. Espinosa, A. Curcio, S. Cabana, G. Radtke, M. Bugnet, J. Kolosnjaj-Tabi, C. Pechoux, C. Alvarez-Lorenzo, G.A. Botton, A.K.A. Silva, A. Abou-Hassan, C. Wilhelm, Intracellular biodegradation of ag nanoparticles, storage in ferritin, and protection by a au shell for enhanced photothermal therapy, ACS Nano 12 (2018) 6523–6535.
[12] M. Chen, S. Tang, Z. Guo, X. Wang, S. Mo, X. Huang, G. Liu, N. Zheng, Core-shell Pd@Au nanoplates as theranostic agents for in-vivo photoacoustic imaging, CT imaging, and photothermal therapy, Adv. Mater. 26 (2014) 8210–8216.
[13] C.M. Hessel, V.P. Pattani, M. Rasch, M.G. Panthani, B. Koo, J.W. Tunnell, B.A. Korgel, Copper selenide nanocrystals for photothermal therapy, Nano Lett. 11 (2011) 2560–2566.
[14] X. Wang, F. Lv, T. Li, Y. Han, Z. Yi, M. Liu, J. Chang, C. Wu, Electrospun micropatterned nanocomposites incorporated with Cu_2S nanoflowers for skin tumor therapy and wound healing, ACS Nano 11 (2017) 11337–11349.
[15] H.K. Moon, S.H. Lee, H.C. Choi, In vivo near-infrared mediated tumor destruction by photothermal effect of carbon nanotubes, ACS Nano 3 (2009) 3707–3713.
[16] J.T. Robinson, S.M. Tabakman, Y. Liang, H. Wang, H.S. Casalongue, D. Vinh, H. Dai, Ultrasmall reduced graphene oxide with high near-infrared absorbance for photothermal therapy, J. Am. Chem. Soc. 133 (2011) 6825–6831.
[17] J. Yang, J. Choi, D. Bang, E. Kim, E.K. Lim, H. Park, J.S. Suh, K. Lee, K.H. Yoo, E.K. Kim, Y.M. Huh, S. Haam, Convertible organic nanoparticles for near-infrared photothermal ablation of cancer cells, Angew. Chem. Int. Ed. Engl. 50 (2011) 441–444.
[18] J.F. Lovell, C.S. Jin, E. Huynh, H. Jin, C. Kim, J.L. Rubinstein, W.C. Chan, W. Cao, L.V. Wang, G. Zheng, Porphysome nanovesicles generated by porphyrin bilayers for use as multimodal biophotonic contrast agents, Nat. Mater. 10 (2011) 324–332.
[19] J.F. Lovell, C.S. Jin, E. Huynh, T.D. MacDonald, W. Cao, G. Zheng, Enzymatic regioselection for the synthesis and biodegradation of porphysome nanovesicles, Angew. Chem. Int. Ed. Engl. 51 (2012) 2429–2433.
[20] W. Cheng, J. Nie, N. Gao, G. Liu, W. Tao, X. Xiao, L. Jiang, Z. Liu, X. Zeng, L. Mei, A multifunctional nanoplatform against multidrug resistant cancer: merging the best of targeted chemo/gene/photothermal therapy, Adv. Funct. Mater. 27 (2017) 1704135.
[21] X. Zeng, M. Luo, G. Liu, X. Wang, W. Tao, Y. Lin, X. Ji, L. Nie, L. Mei, Polydopamine-modified black phosphorous nanocapsule with enhanced stability and photothermal performance for tumor multimodal treatments, Adv. Sci. 5 (2018) 1800510.
[22] A. Nel, T. Xia, L. Madler, N. Li, Toxic potential of materials at the nanolevel, Science 311 (2006) 622–627.
[23] S. Sharifi, S. Behzadi, S. Laurent, M.L. Forrest, P. Stroeve, M. Mahmoudi, Toxicity of nanomaterials, Chem. Soc. Rev. 41 (2012) 2323–2343.
[24] J.D. Simon, Spectroscopic and dynamic studies of the epidermal chromophores trans-urocanic acid and eumelanin, Acc. Chem. Res. 33 (2000) 307–313.
[25] Y. Li, C. Jiang, D. Zhang, Y. Wang, X. Ren, K. Ai, X. Chen, L. Lu, Targeted polydopamine nanoparticles enable photoacoustic imaging guided chemo-photothermal synergistic therapy of tumor, Acta Biomater. 47 (2017) 124–134.
[26] S. Liu, J. Pan, J. Liu, Y. Ma, F. Qiu, L. Mei, X. Zeng, G. Pan, Dynamically pegylated and borate-coordination-polymer-coated polydopamine nanoparticles for synergetic tumor-targeted, chemo-photothermal combination therapy, Small 14 (2018) e1703968.
[27] G. von Maltzahn, J.H. Park, A. Agrawal, N.K. Bandaru, S.K. Das, M.J. Sailor, S.N. Bhatia, Computationally guided photothermal tumor therapy using long-circulating gold nanorod antennas, Cancer Res. 69 (2009) 3892–3900.
[28] E. Paulet, C. Aube, P. Pessaux, J. Lebigot, E. Lhermitte, F. Oberti, A. Ponthieux, P. Cales, C. Ridereau-Zins, P.L. Pereira, Factors limiting complete tumor ablation by radiofrequency ablation, Cardiovasc. Intervent. Radiol. 31 (2008) 107–115.
[29] L. Dong, Y. Li, Z. Li, N. Xu, P. Liu, H. Du, Y. Zhang, Y. Huang, J. Zhu, G. Ren, J. Xie, K. Wang, Y. Zhou, C. Shen, J. Zhu, J. Tao, Au nanocage-strengthened dissolving microneedles for chemo-photothermal combined therapy of superficial skin tumors, ACS Appl. Mater. Interfaces 10 (2018) 9247–9256.
[30] Y. Wang, X. Ji, P. Pang, Y. Shi, J. Dai, J. Xu, J. Wu, T.B. Kirk, W. Xue, Synthesis of Janus Au nanorods/polydivinylbenzene hybrid nanoparticles for chemo-photothermal therapy, J. Mater. Chem. B 6 (2018) 2481–2488.
[31] Y. Wang, X. Liu, G. Deng, J. Sun, H. Yuan, Q. Li, Q. Wang, J. Lu, Se@SiO_2-fa-CuS nanocomposites for targeted delivery of dox and nano selenium in synergistic combination of chemo-photothermal therapy, Nanoscale 10 (2018) 2866–2875.
[32] M. Yao, Y. Ma, H. Liu, M.I. Khan, S. Shen, S. Li, Y. Zhao, Y. Liu, G. Zhang, X. Li, F. Zhong, W. Jiang, Y. Wang, Enzyme degradable hyperbranched polyphosphoester micellar nanomedicines for nir imaging-guided chemo-photothermal therapy of drug-resistant cancers, Biomacromolecules 19 (2018) 1130–1141.
[33] Y. Peng, J. Nie, W. Cheng, G. Liu, D. Zhu, L. Zhang, C. Liang, L. Mei, L. Huang, X. Zeng, A multifunctional nanoplatform for cancer chemo-photothermal synergistic therapy and overcoming multidrug resistance, Biomater. Sci. 6 (2018) 1084–1098.
[34] L. Feng, X. Yang, X. Shi, X. Tan, R. Peng, J. Wang, Z. Liu, Polyethylene glycol and polyethylenimine dual-functionalized nano-graphene oxide for photothermally enhanced gene delivery, Small 9 (2013) 1989–1997.
[35] C. Wang, H. Xu, C. Liang, Y.M. Liu, Z.W. Li, G.B. Yang, H. Cheng, Y.G. Li, Z. Liu, Iron oxide @ polypyrrole nanoparticles as a multifunctional drug carrier for remotely controlled cancer therapy with synergistic antitumor effect, ACS Nano 7 (2013) 6782–6795.
[36] B. Hildebrandt, P. Wust, O. Ahlers, A. Dieing, G. Sreenivasa, T. Kerner, R. Felix, H. Riess, The cellular and molecular basis of hyperthermia, Crit. Rev. Oncol. Hematol. 43 (2002) 33–56.
[37] M.J. Alonso, Nanomedicines for overcoming biological barriers, Biomed. Pharmacother. 58 (2004) 168–172.
[38] X. Guo, C. Shi, G. Yang, J. Wang, Z. Cai, S. Zhou, Dual-responsive polymer micelles for target-cell-specific anticancer drug delivery, Chem. Mater. 26 (2014) 4405–4418.
[39] H. Koo, M.S. Huh, I.C. Sun, S.H. Yuk, K. Choi, K. Kim, I.C. Kwon, In vivo targeted delivery of nanoparticles for theranosis, Acc. Chem. Res. 44 (2011) 1018–1028.
[40] D. Liu, D.T. Auguste, Cancer targeted therapeutics: From molecules to drug delivery vehicles, J. Controlled Release 219 (2015) 632–643.
[41] A. Albanese, P.S. Tang, W.C. Chan, The effect of nanoparticle size, shape, and surface chemistry on biological systems, Annu. Rev. Biomed. Eng. 14 (2012) 1–16.
[42] R. De Souza, P. Zahedi, C.J. Allen, M. Piquette-Miller, Polymeric drug delivery systems for localized cancer chemotherapy, Drug Deliv. 17 (2010) 365–375.
[43] S. Talebian, J. Foroughi, S.J. Wade, K.L. Vine, A. Dolatshahi-Pirouz, M. Mehrali, J. Conde, G.G. Wallace, Biopolymers for antitumor implantable drug delivery systems: recent advances and future outlook, Adv. Mater. (2018) e1706665.
[44] A. Aguayo, Y.Z. Patt, Nonsurgical treatment of hepatocellular carcinoma, Semin. Oncol. 28 (2001) 503–513.
[45] W.C. Su, W.W. Lai, H.H. Chen, T.R. Hsiue, C.W. Chen, W.T. Huang, T.Y. Chen, C.J. Tsao, N.S. Wang, Combined intrapleural and intravenous chemotherapy, and pulmonary irradiation, for treatment of patients with lung cancer presenting with malignant pleural effusion. A pilot study, Oncology 64 (2003) 18–24.
[46] E.P. Goldberg, A.R. Hadba, B.A. Almond, J.S. Marotta, Intratumoral cancer chemotherapy and immunotherapy: Opportunities for nonsystemic preoperative drug delivery, J. Pharm. Pharmacol. 54 (2002) 159–180.

[47] J. Yang, Y. Wu, Y. Shen, C. Zhou, Y.F. Li, R.R. He, M. Liu, Enhanced therapeutic efficacy of doxorubicin for breast cancer using chitosan oligosaccharide-modified halloysite nanotubes, ACS Appl. Mater. Interfaces 8 (2016) 26578–26590.
[48] B.D. Weinberg, H. Ai, E. Blanco, J.M. Anderson, J. Gao, Antitumor efficacy and local distribution of doxorubicin via intratumoral delivery from polymer millirods, J. Biomed. Mater. Res. A 81 (2007) 161–170.
[49] P. Agarwal, I.D. Rupenthal, Injectable implants for the sustained release of protein and peptide drugs, Drug Discov. Today 18 (2013) 337–349.
[50] A. Fakhari, J. Anand, Subramony, Engineered in-situ depot-forming hydrogels for intratumoral drug delivery, J. Controlled Release 220 (2015) 465–475.
[51] P. Menei, E. Jadaud, N. Faisant, M. Boisdron-Celle, S. Michalak, D. Fournier, M. Delhaye, J.P. Benoit, Stereotaxic implantation of 5-fluorouracil-releasing microspheres in malignant glioma, Cancer 100 (2004) 405–410.
[52] L. Yu, X.Y. Yu, X.W.D. Lou, The design and synthesis of hollow micro-/nanostructures: present and future trends, Adv. Mater. 30 (2018) e1800939.
[53] A. Pawar, S. Thakkar, M. Misra, A bird's eye view of nanoparticles prepared by electrospraying: advancements in drug delivery field, J. Controlled Release 286 (2018) 179–200.
[54] S. Zhou, X. Deng, X. Li, Investigation on a novel core-coated microspheres protein delivery system, J. Controlled Release 75 (2001) 27–36.
[55] G. Yang, X. Li, Y. He, X. Xiong, P. Wang, S. Zhou, Capturing circulating tumor cells through a combination of hierarchical nanotopography and surface chemistry, ACS Biomater. Sci. Eng. 4 (2017) 2081–2088.
[56] N. Bock, T.R. Dargaville, M.A. Woodruff, Electrospraying of polymers with therapeutic molecules: state of the art, Progr. Polym. Sci. 37 (2012) 1510–1551.
[57] X.-X. Wang, X.J. Ju, S.X. Sun, R. Xie, W. Wang, Z. Liu, L.Y. Chu, Monodisperse erythrocyte-sized and acid-soluble chitosan microspheres prepared via electrospraying, RSC Adv. 5 (2015) 34243–34250.
[58] L. Zhang, T. Si, A.J. Fischer, A. Letson, S. Yuan, C.J. Roberts, R.X. Xu, Coaxial electrospray of ranibizumab-loaded microparticles for sustained release of anti-VEGF therapies, PLoS One 10 (2015) e0135608.
[59] F. Liu, X. He, Z. Lei, L. Liu, J. Zhang, H. You, H. Zhang, Z. Wang, Facile preparation of doxorubicin-loaded upconversion@polydopamine nanoplatforms for simultaneous in vivo multimodality imaging and chemophotothermal synergistic therapy, Adv. Healthcare Mater. 4 (2015) 559–568.
[60] L. Liu, J.-P. Yang, X.-J. Ju, R. Xie, Y.-M. Liu, W. Wang, J.-J. Zhang, C.H. Niu, L.-Y. Chu, Monodisperse core-shell chitosan microcapsules for pH-responsive burst release of hydrophobic drugs, Soft Matter. 7 (2011) 4821–4827.
[61] S.K. Parks, J. Chiche, J. Pouyssegur, Disrupting proton dynamics and energy metabolism for cancer therapy, Nat. Rev. Cancer 13 (2013) 611–623.
[62] S.B. Zhou, X.M. Deng, X.H. Li, W.X. Jia, L. Liu, Synthesis and characterization of biodegradable low molecular weight aliphatic polyesters and their use in protein-delivery systems, J. Appl. Polym. Sci. 91 (2004) 1848–1856.
[63] Y.H. Bae, K. Park, Targeted drug delivery to tumors: Myths, reality and possibility, J. Controlled Release 153 (2011) 198–205.
[64] S. Wilhelm, A.J. Tavares, Q. Dai, S. Ohta, J. Audet, H.F. Dvorak, W.C.W. Chan, Analysis of nanoparticle delivery to tumours, Nat. Rev.s Mater. 1 (2016) 16014.
[65] F. Zhou, S. Wu, B. Wu, W.R. Chen, D. Xing, Mitochondria-targeting single-walled carbon nanotubes for cancer photothermal therapy, Small 7 (2011) 2727–2735.